Electron-Beam Induced Luminescence and Bleaching in Polymer Resins and Embedded Biomaterial

Srinivasa Raja, Aditi; de Boer, Pascal; Giepmans, Ben N.G.; Hoogenboom, Jacob P.

DOI
10.1002/mabi.202100192

Publication date
2021

Document Version
Final published version

Published in
Macromolecular Bioscience

RESEARCH ARTICLE

Macromolecular Bioscience
www.mbs-journal.de

Electron-Beam Induced Luminescence and Bleaching in Polymer Resins and Embedded Biomaterial

*Aditi Srinivasa Raja, Pascal de Boer, Ben N. G. Giepmans, and Jacob P. Hoogenboom**

Electron microscopy is crucial for imaging biological ultrastructure at nanometer resolution. However, electron irradiation also causes specimen damage, reflected in structural and chemical changes that can give rise to alternative signals. Here, luminescence induced by electron-beam irradiation is reported across a range of materials widely used in biological electron microscopy. Electron-induced luminescence is spectrally characterized in two epoxy (Epon, Durcupan) and one methacrylate resin (HM20) over a broad electron fluence range, from 10^{-4} to 10^{3} mC cm^{-2}, both with and without embedded biological samples. Electron-induced luminescence is pervasive in polymer resins, embedded biomaterial, and occurs even in fixed, whole cells in the absence of resin. Across media, similar patterns of intensity rise, spectral red-shifting, and bleaching upon increasing electron fluence are observed. Increased landing energies cause reduced scattering in the specimen shifting the luminescence profiles to higher fluences. Predictable and tunable electron-induced luminescence in natural and synthetic polymer media is advantageous for turning many polymers into luminescent nanostructures or to fluorescently visualize (micro)plastics. Furthermore, these findings provide perspective to direct electron-beam excitation approaches like cathodoluminescence that may be obscured by these nonspecific electron-induced signals.

1. Introduction

Electron microscopy (EM) is key in biology to image the ultrastructural layout of cells and tissues with a typical resolution equal to the sizes of macromolecules.[1] However, electron-beam irradiation during EM acquisition also leads to structural changes, molecular rearrangements, and degradation.[2–4] Cross linking, chain scission, unsaturation, and gas emission are examples of chemical processes that can subsequently occur. The resultant loss of structural integrity limits the tolerable electron dose and may give rise to dose-dependent distortions, such as local shrinkage. Characterization of these effects on biological specimens and the polymer resins typically used to embed tissues or cellular samples for EM, has largely been restricted to observing this shrinkage, or the accompanying shape changes and mass loss.[5,6] Here, we show that electron-beam irradiation incites luminescence in biological media and their embedding resins with strikingly similar patterns of electronfluence dependent intensity rise, spectral red-shift, and bleaching across materials.

Luminescence as a particular outcome of irradiation has been reported across multiple polymers, with plastic scintillators as a potent example.[7–9] Recently, electron-irradiation induced luminescence has been reported for fabrication of polymethylmethacrylate (PMMA), polystyrene (PS), polyacrylamide, and poly(3-methylthiophene) nanostructures with tunable optical properties.[10–13]

Interestingly, recent reports on electron-irradiation of fluorescent proteins show electron-enhanced fluorescence and cathodoluminescence (CL) that is robust under electron-irradiation.[14,15] This could hold great promise for high-resolution multimodal microscopy but it also raises the question whether luminescence can be more generally induced during EM in biological samples and their embedding polymer resins.

In this work, we carried out a detailed characterization of electron-luminescence in materials typically used for biological EM. We find that electron-induced luminescence grows in intensity, reaches a peak and bleaches with increasing electron fluence. This is further accompanied by spectral broadening and red-shifting. Moreover, induced luminescence shows intensity variations between compact material and embedded tissue within the same sample. We further discuss how such electron-induced luminescence may affect high-resolution approaches to identify small biomolecular probes via CL, stressing the importance of choosing the right spectral settings that do not overlap with the induced luminescence spectra.

A. Srinivasa Raja, J. P. Hoogenboom
Department of Imaging Physics
Delft University of Technology
Delft 2628 CJ, The Netherlands
E-mail: j.p.hoogenboom@tudelft.nl
P. de Boer, B. N. G. Giepmans
Department of Biomedical Sciences of Cells and Systems
University of Groningen, University Medical Center Groningen
Groningen 9713 GZ, The Netherlands

The ORCID identification number(s) for the author(s) of this article can be found under https://doi.org/10.1002/mabi.202100192

DOI: 10.1002/mabi.202100192

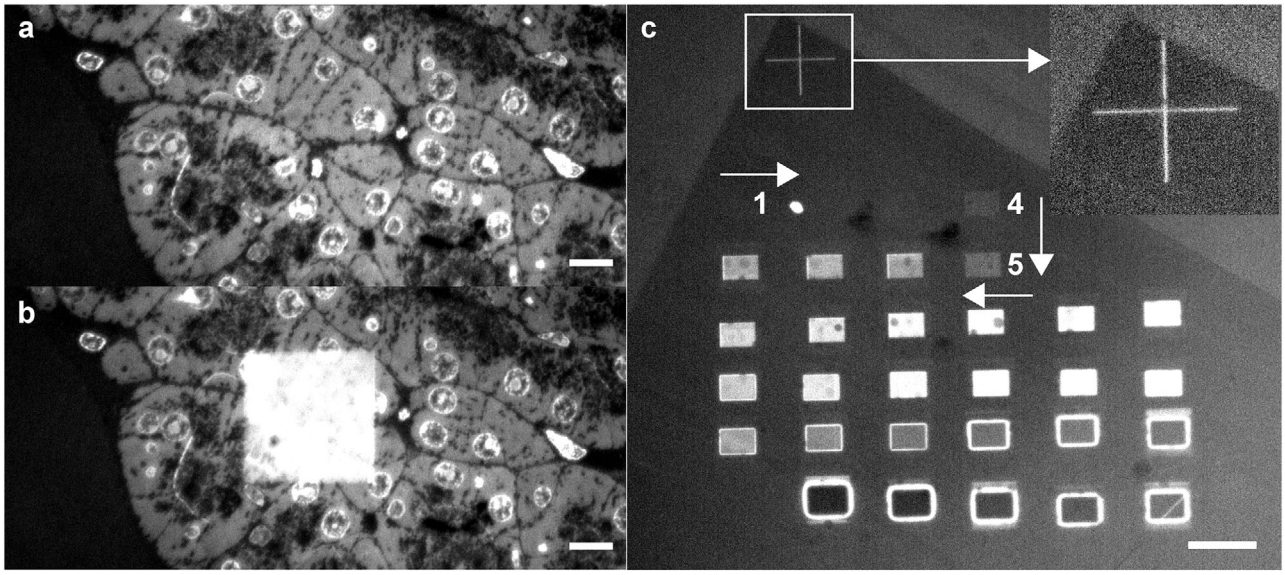

Figure 1. Electronfluence dependent induced luminescence in EM samples shows dynamic rise and decay. Hoechst signal of 80 nm Epon embedded tissue section a) before and b) after electron-beam exposure. c) Electron fluence exposure series on HM20 embedded HeLa cells. Rectangular areas were exposed to increasing electron fluence from the top-left (starting from 1, continuing through 4–5) in a meandering fashion as indicated by the arrows. The luminescent cross was made with a focused electron-beam to aid in region-of-interest retrieval. a–c) Excitation: 405 nm; emission multi-band filters: 432/515/595/730-25 nm. Bars: 10 μm (a,b); 100 μm (c).

2. Results and Discussion

2.1. Luminescence in EM Prepared Materials after Irradiation

Electron irradiation-induced luminescence is best illustrated upon fluorescent imaging of an area exposed to a focused electron-beam (**Figure 1**). A typical EM biological sample, 80 nm thin section of Epon embedded rat pancreas, was counterstained with Hoechst and imaged on a fluorescence microscope (Figure 1a). Strikingly, the exposed area shows bright luminescence that overwhelms the original signal after EM analysis as shown in Figure 1b. To address whether this phenomenon is characteristic of Epon, we subjected three unstained resins, with and without embedded biomaterial, to controlled exposures of increasing electron fluence (Figure 1c) in a scanning electron microscope (SEM). The three resins are representative for (typically epoxy or acrylic-based) EM-resins: besides Epon, epoxy-based Durcupan, and acrylic-based HM20. In EM, the choice of resin would be dictated by the requirement: Epon has excellent sectioning qualities, HM20 is hydrophilic and suited for immunocytochemistry, while Durcupan is a low-viscosity, water-soluble epoxy variant.

All specimens were exposed at 1 and 5 kV landing energies with fluence in the range of 10^{-4} to 10^{3} mC cm^{-2}. We find that upon increasing fluence, luminescence is induced, then rises, and subsequently bleaches. When the exposed area is bleached, the intensity in the surrounding region increases due to proximity exposure, leading to a halo. Note that we advantageously used the same phenomenon of electron-induced luminescence to mark the exposed areas (inset in Figure 1c) to navigate in the fluorescence mode toward the areas of interest, especially the regions that showed negligible luminescence (areas 1 to 4).

To understand induced luminescence dynamics, we quantified the emission behavior as it varies with electron fluence. The total luminescence intensity as a function of fluence was obtained for three resins, Epon, Durcupan, and HM20, both with and without biological material (**Figure 2**). The applied fluences were controlled by both varying the current and the dwell time. Hence, the results are only indicative of the total integrated fluence. UV–Vis spectral characterization was carried out in an independent laser scanning confocal system, where the marker in Figure 1c aided in navigation and region of interest retrieval. Standard excitation wavelengths were applied (405, 488, 561, 594, and 633nm). Emission was recorded between 414 and 690 nm in 9 nm intervals and summed together. We find electron-beam induced luminescence i) in all examined resins, ii) irrespective of the biomaterial within resins, iii) the global trend is a rise and subsequent decay and is similar for all samples, iv) modulation is contained within 10^{-2} to 10^{2} mC cm^{-2}, and v) the overall emission intensity per excitation wavelength is highest at 405 nm and progressively weakens at higher wavelengths emissions. Thus, none of the three examined resins remains inert to electron exposure. The addition of biomaterial does not significantly alter the general trends. The fluence range, spanning four orders of magnitude, indicates that this luminescent phenomenon is a long-drawn effect that cannot be circumvented unless imaging is restricted to low electron fluences ($<10^{-2}$ mC cm^{-2}). We also note that induced luminescence is an enduring effect. Owing to sample transfer requirements, spectroscopic analysis was typically carried out 1–2 weeks after electron exposure. The resulting data align with the patterns observed in preliminary fluorescence inspection as seen in Figure 1c.

We next investigate the relation between the induced luminescence and the a priori present autofluorescence. Autofluorescence contributes to the detected intensities as a starting background level for all samples (Figure 2), but is most pronounced for bare Epon. Up to 10^{-2} mC cm^{-2}, autofluorescence remains the main contributor to the detected signal, after which

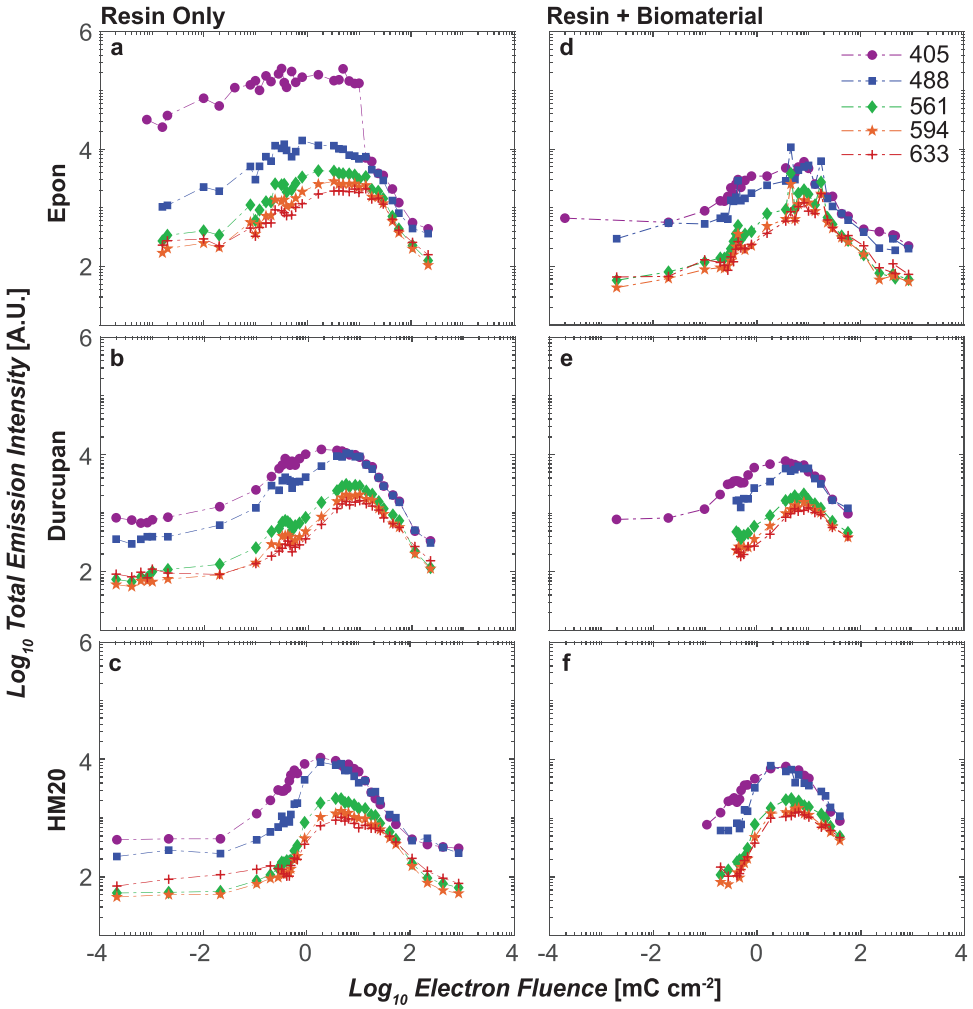

Figure 2. Electron-induced luminescence increases, red-shifts, and bleaches with increasing electron fluence. Total electron-beam induced luminescence emission intensity as a function of fluence. Colors indicate excitation wavelengths as indicated. (a–c) bare resins and (d–f) samples with embedded biomaterial, namely, rat pancreas tissue (d) or HeLa cells (e,f). All data were recorded with 1 keV electron landing energy. Note that bare Epon already shows high UV-excited autofluorescence before electron irradiation. Electron-induced luminescence occurs for all resins, with an intensity increase followed by decay.

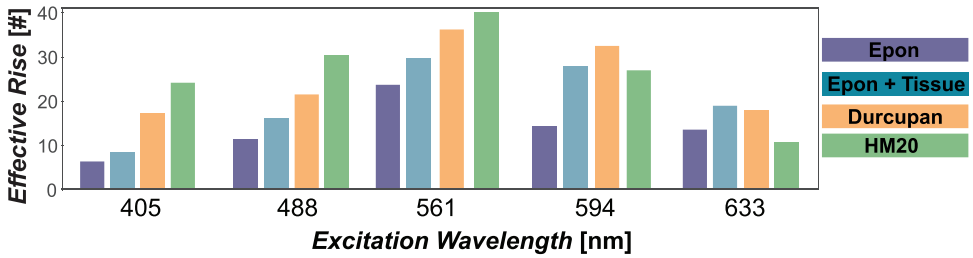

Figure 3. Electron-beam induced fluorescence on top of resin autofluorescence. Effective rise in electron-beam induced luminescence relative to native autofluorescence at the respective excitation wavelengths. The rise in electron-induced signal is strongest at 561 nm.

electron-beam induced luminescence starts to increase. Autofluorescence emission spectra are broad-banded and most pronounced in the blue regime. However, the cumulative rise in detected signal strictly due to electron-beam exposure is most pronounced in the green regime, with a 20–40-fold increase (**Figure 3**).

The variation of electron-induced luminescence with electron fluence is particularly important for CL, in which a luminescent probe is excited by a focused electron-beam. CL signals are typically weak due to a low cross-section and quantum yield compared to, e.g., photon-excited fluorescence. As a result, most reported CL active probes are relatively large (40–200

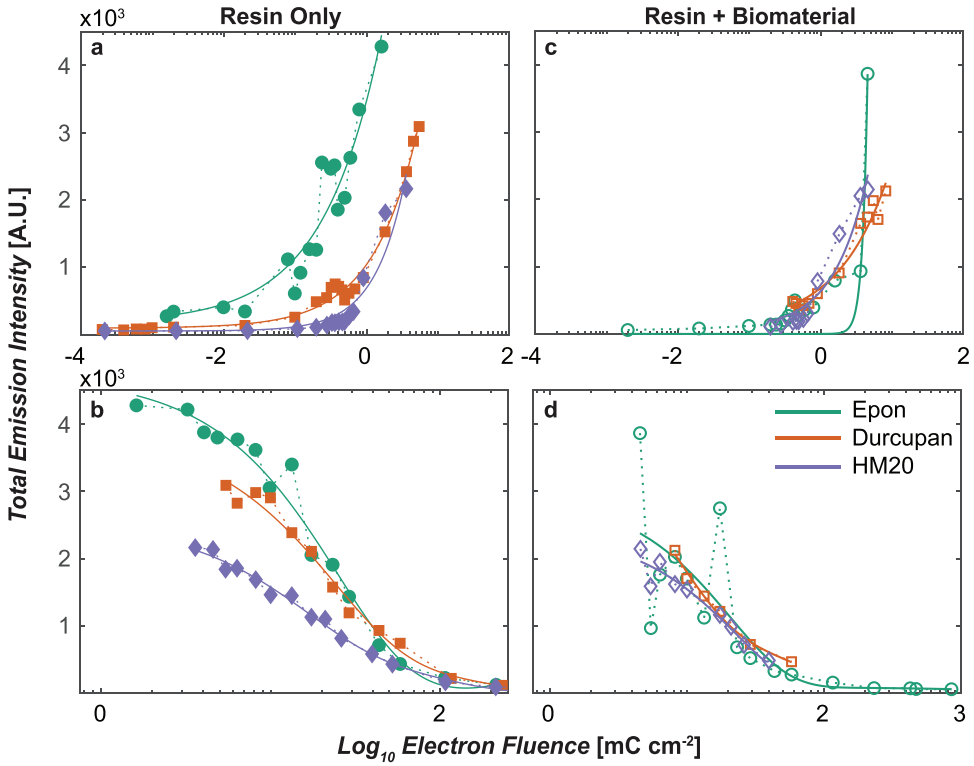

Figure 4. Luminescence rise and bleach curves fall in similar fluence magnitude regimes across samples. a) The rise in electron-induced luminescence for all bare resins as indicated (excitation: 561 nm) as a function of electron fluence. b) The decay in luminescence in the bleaching regime. c,d) Similar curves for the resins with embedded biomaterials. Symbols indicate measured values; solid lines indicate fit with a power-law and double-exponential function for the rise and bleach regime respectively. In all cases, the induced luminescence rises between 10^{-3} and 5 mC cm^{-2}, and decays between 5 and 100 mC cm^{-2}. Full curves for all excitation wavelengths and materials can be found in the Supporting Information.

nm),[16–18] but sub-20 nm[19] CL nanoparticles have recently been reported. These smaller CL probes better fit applications in cells and tissues, while also allowing higher resolution detection, but electron-induced luminescence background could obscure the probe signal. While a CL probe may be observable at low electron fluence, i.e., low magnification, higher fluence for higher magnification examination may drown the CL signals in the electron-induced background. Signal-to-background estimates must therefore factor in the rise and bleaching of induced luminescence as the cumulative electron fluence changes due to either increased magnification or repeated inspection. We therefore analyze the rise, decay and spectral evolution of electron-induced luminescence in our samples in more detail.

2.2. Luminescence Increase, Red-Shift, and Bleaching

The luminescence rise and subsequent bleaching with increasing electron fluence occurs in a similar fluence range for all tested resins, exemplified for 561 nm excitation (**Figure 4**). A steep rise is observed between 1 μC cm^{-2} and 2 mC cm^{-2}. Bleaching commences a few mC cm^{-2} later and continues until about 100 mC cm^{-2}, when the exposed area has faded completely. Both processes are markedly nonlinear: rise and bleach curves are best fit to power-law and double-exponential functions, respectively. Only in specific cases and in a limited fluence interval, the rise can be approximated as linear, e.g., for HM20 at excitation wavelengths between 561 and 633 nm. While all three resins qualitatively display the same behavior, HM20 shows the largest increase with respect to native auto-fluorescence between 405 and 561 excitation (Figure 3). However, the bare HM20 also has the lowest peak intensity across all excitation wavelengths and the narrowest activation range in terms of electron fluence, making it a suitable choice if a low-background bare resin is required (Figure 4a,b; Figure S1a–l, Supporting Information).

Bare resins do not possess compositional variations from the embedded biological specimens. Yet, real EM samples contain biomaterial, occasionally with empty resin areas within. We therefore examined bare resin and bioembedded regions separately to account for their individual luminescence contributions (Figure 4c,d; Figure S1a–j, Supporting Information). The replacement of resin by fixed biomaterial (low autofluorescence) reduces induced luminescence. In addition, fixation and staining chemicals (aldehydes, osmium tetroxide, and potassium ferrocyanide) could potentially downregulate the high intensities as observed with pure resin. Similar behavior is observed for the autofluorescence of Epon (Figure 2a,d). Thus, while biological specimens are themselves autofluorescent, their luminescence contribution is lower than resin and is possibly less UV excitable and/or with a lower quantum yield. Note that Epon embedded pancreas shows larger fluctuations in measured intensity per fluence. We attribute this to density differences between the exocrine and the

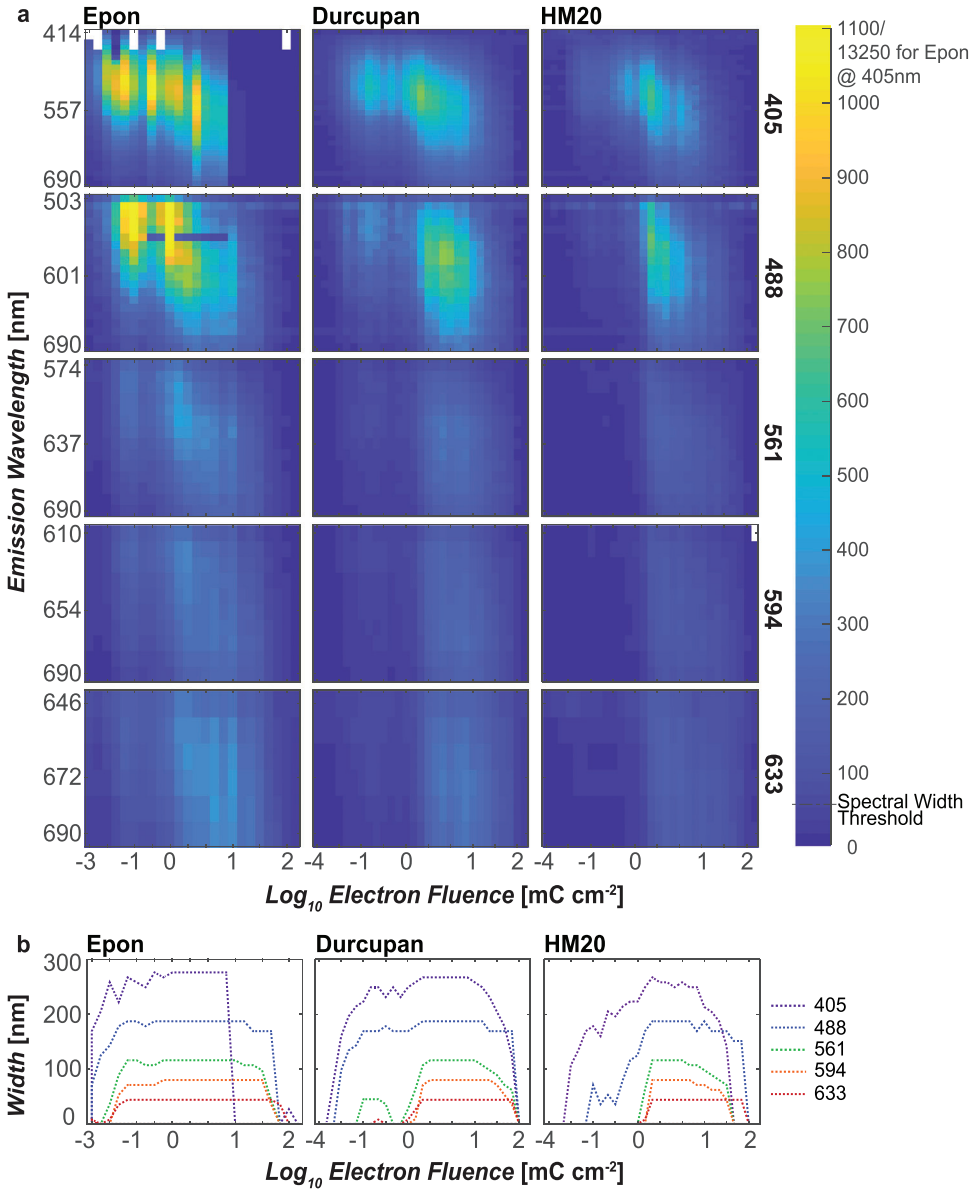

Figure 5. Electron-induced luminescence spectrum shifts from blue to red upon increasing electron fluence. a) Color-coded luminescence emission intensity as a function of electron fluence for each of the different excitation wavelengths indicated right. White pixels denote missing values. b) Spectral width as a function of electron fluence for each excitation wavelength and resin. The spectral width has been defined as the range in which the threshold intensity indicated in the color scale in (a) is exceeded. The threshold (725 for bare Epon and 60 units for the rest) is set slightly above the highest autofluorescence values. The induced luminescence spectrum broadens and red-shifts upon increasing exposure until it spans the entire visible range and then narrows again upon bleaching.

materially denser endocrine regions and that prior to exposure, we have no means to discriminate the two. For Durcupan and HM20 embedded with HeLa cells, all data is from the cytoplasm. Importantly, we see that the observed changes in induced luminescence intensity will be more dependent on density variations in the embedded sample than in the chosen resin.

Spectral characterization of induced luminescence is critical to identify emission windows that permit background filtering. Comparison of induced luminescence per excitation wavelength (Figure 3) suggests that the spectrum red-shifts with increasing fluence. Orange and red wavelengths still experience an increase in induced luminescence while UV and blue excitations already decay. This is confirmed by a full spectral analysis (**Figure 5**). For all three resins, the emission spectrum broadens and red-shifts upon increasing electron irradiation. For 405 nm excitation, where the full 414–690 nm range is analyzed for emission, we observe three patterns. i) At low fluence, induced emission begins at low intensities between 420 and 575 nm. There is no clear spectral peak, but the spectral center of mass is at 503–512 nm. ii) Upon increasing electron fluence, the emission

increases, and the spectrum develops a peak in the above range. The spectral width has now broadened into the red part of the spectrum, covering the entire measured range. iii) When the overall intensity bleaches, the spectral peak skews to orange-red wavelengths while the width progressively narrows until it settles below background levels. Bare Epon deviates from the rest in its high UV excited autofluorescence. This shows a sharp drop at ≈10 mC cm−^{2} to the intensity values also observed at 488 nm excitation, suggesting damage to the UV excitable component. The higher excitations show a threshold at ≈1 mC cm^{-2} below which effective excitation only occurs in the UV. 488 nm shows diminished emission around this fluence and this is further lowered between 561 and 633 nm. The same behavior is observed for resins with embedded biological material (Figure S2, Supporting Information). Only in the case of bare Epon, the reduction in intensity at higher wavelengths is less pronounced. In addition to red-shifting, a subtle increase in red wavelength emission is also observed with increasing excitation. The fact that the spectrum ultimately extends over the full range is further confirmed by analyzing the spectral range where the emission exceeds a set threshold level (Figure 5b).

2.3. Electron Energy Dependence

In addition to electron fluence, we examined the influence of electron-beam primary energy on induced luminescence. At 1 keV landing energy, the interaction volume is contained within the ≈80 nm thickness of our specimen. Thus, the total number of scattering events is encapsulated in the specimen, providing a direct relationship between the fluence and the ensuing luminescence. With 5 keV landing energy, we retrieve the same behavior for induced luminescence, albeit shifted to larger fluence (Figure S3, Supporting Information). At 5 keV, a significant portion of the interaction volume falls into the sample support. Thus, a fraction of the primary electrons exits the section without scattering and consequently, the threshold fluence for luminescence induction is higher. In addition, we note that at 1 keV the distribution of secondary electrons and that generated by back-scattered electrons (BSE), namely, SE2's is similar, thereby tightly localizing the damage to the scanned regions. At 5 keV or higher energy, the BSE and SE2's will have a broader distribution area. With higher fluence, the cumulative rise in fluence in these delocalized areas will incite luminescence. The effect is thus a central bleached region, similar to that of 1 keV but with a luminescent perimeter (see Figure 2). The fact that induced luminescence is a by-product of the density of low energy scattering events is reflected at the fluence at which maximum intensity is reached (Figure S3, Supporting Information). Epon, Durcupan, and HM20 reach peak intensity at ≈0.30, 1.8, and 1.8 mC cm^{-2} at 1 keV irradiation and 405 nm excitation, respectively. This is shifted to ≈1.6, 3.6, and 6.0 mC cm^{-2} at 5 keV irradiation. Similar patterns in radiation damage as a function of specimen thickness, relative to the landing energy has been shown.[20] Since electron-induced damage is predominantly caused by low energy secondary electrons, we point out that 1 keV irradiation of a material with a higher secondary electron coefficient is expected to luminesce at lower fluence.

2.4. Electron-Induced Luminescence in Biological Materials

The electron-induced luminescence is not restricted to resins only but also shows variations within biological materials itself. We noted differences between exocrine and endocrine regions in Epon embedded rat pancreas tissue which we attributed to changes in biomaterial density. This is exemplified where an electron-beam scan area crosses the boundary between bare and tissue embedding Epon resin (**Figure 6**). For the same fluence, bare resin shows higher induced luminescence than the tissue regions. However, in tissue, nuclei appear brighter than the cytoplasm (Figure 6b). Note that the entire nuclei stand out in induced luminescence and not merely the Hoechst expressing regions that are visible in Figure 6a. Figure 6c,d reports total induced luminescence differences between the cytoplasm and nucleus from unstained Epon sections, which indicate that a slightly higher luminescence is reached in the nucleus at similar fluence. This corroborates the notion that reactions in and between organic macromolecules and polymers are responsible for the induced luminescence. Thus, regions dense in biological macromolecules, like the nucleus,[21] will stand out in electron-induced luminescence.

Remarkably, electron-beam induced luminescence is also observed in resin-free HeLa cells (**Figure 7**). Even in the absence of any resin, electron-induced luminescence persists, rises, and subsequently bleaches at high fluence (Figure 7a from left to right). The scanned regions also follow similar spectral tendencies, indicated for both 470 and 555 nm for low (Figure 7b) and high fluence (Figure 7c), respectively. Low fluence shows minimal induction of luminescence at 470 nm and no discernible induced luminescence at 555 nm (Figure 7b), in correspondence with our observations on the resins (Figure 5). Higher electron fluence induces stronger luminescence, which can now also be excited with 555 nm (Figure 7c). This confirms that native organic biological materials, in this case possibly in combination with the aldehyde fixatives, show the same trends in electron-induced luminescence as the polymer resins.

Though electron-induced luminescence appears to reveal previously unseen cellular contrast, we attribute the resultant contrast to varying effective dose in regions with material differences. Figure 7a shows nonuniform luminescence toward the bottom right of the exposed area. Thickness differences in fixed, dried cells can range from tens of microns close to the nucleus, to a few nanometers toward the cell edges. Electron-beam irradiation with fixed landing energy, and thus interaction depth, thus leads to a luminescence profile that is enhanced in the thicker parts. The nucleus, where both thickness and macromolecular density increase indeed shows strongest electron-induced luminescence signal. The highest fluence exposure illustrates electron scattering proximity exposure (rightmost panel in Figure 7a): the exposed area is bleached, but flanked by a thin luminescent periphery, again highlighting that fixed cells shows the same qualitative behavior as the bare and embedding resins.

2.5. Comparison to PS and PMMA Literature Results

Electron-beam induced luminescence has been reported for nanopatterning fluorescent structures in pure PMMA[10] and

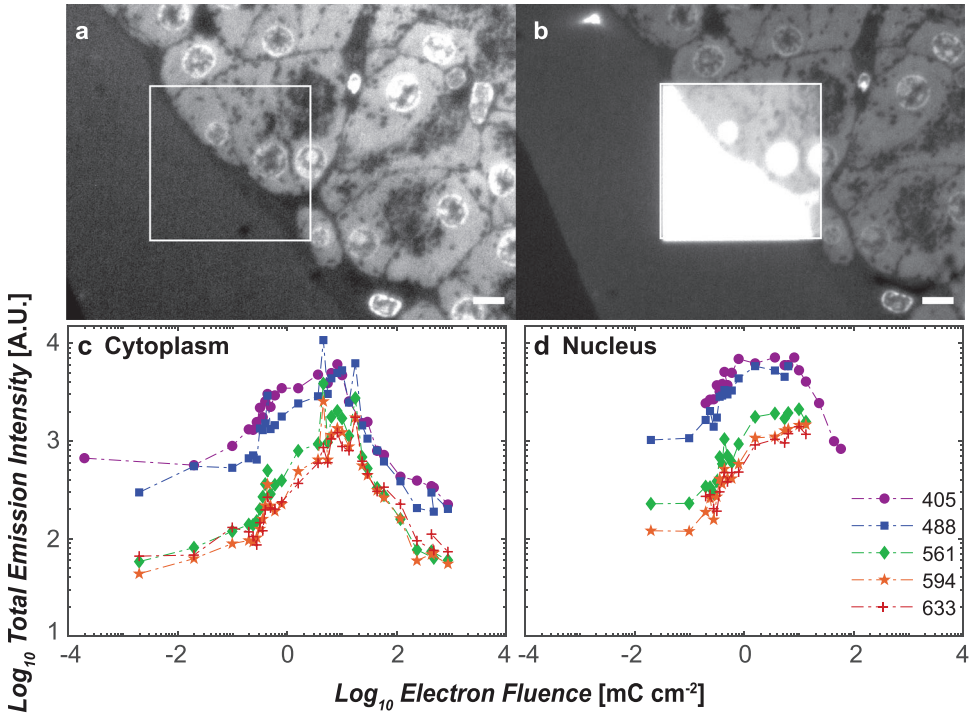

Figure 6. Induced luminescence within the biomaterial correlates with macromolecular density. a) 80 nm Epon embedded Hoechst-stained (DNA, RNA) rat pancreas section, including the boundary between bare resin and tissue. Image recorded with 405 nm excitation before electron irradiation. b) Same image recorded after electron-beam exposure of the boxed area. The scanned area straddles the boundary between the bare resin and rat pancreas tissue. Contrast and brightness adjusted in (b) to highlight induced luminescence variances. The induced luminescence intensity is clearly seen to vary within the biological material despite the same applied fluence. Regions that are denser in macromolecular composition (bare resin, nucleus) appear brighter. c,d) Total luminescence intensity as a function of fluence for (c) cytoplasmic regions and (d) nuclear regions for all excitation wavelengths. Overall, the nuclear regions show higher induced luminescence intensity at the same fluence compared to the cytoplasm. (a,b) Scale bar: 10 µm.

PS.[11] While PS undergoes spectral red-shifting and brodening with increasing fluence, similar to this study, PMMA depicts blue emission which linearly increases in intensity and with no spectral shift or broadening. We compare the PMMA findings with our HM20 results (**Figure 8**), as the latter being a methacrylate resin, still shows spectral red-shifting and broadening which were absent in PMMA.

1 keV data on HM20 cover a similar fluence range as the 50 keV results on PMMA. Between 7 and 25 mC cm^{-2}, HM20 shows decreasing emission, spectral red-shifting, and width narrowing while PMMA reports linearly increasing blue emission in the absence of spectral change. However, the 50 keV PMMA irradiation was conducted with 1 nA on a 500 nm layer, meaning that a substantial portion of the electron fluence is deposited in the polymer. As the differential cross-section of elastic scattering is inversely proportion to the square of the kinetic energy,[22] the scattering cross-section at 50 keV is ≈100 times lower than at 5 keV. Without normalizing for thickness differences, a 100× lower fluence is thus a ball-park estimate. Indeed, comparing the PMMA results to our 5 keV irradiation of HM20 with fluence of 0.002 to 1 mC cm^{-2}, we also observe increasing luminescence intensity and a nearly nonshifting spectrum. Thus, HM20 and the pure PMMA may display the same behavior, only our full data extends over a wider fluence range, from 10^{-4} to 250 mC cm^{-2}, in which the nonlinearity, spectral shifts, and bleaching are observed.

We have reported electron-induced luminescence across a range of materials relevant for biological EM. We have also encountered, but not quantified, electron-induced luminescence effects in materials that do not have biological applications, namely, styrene dyes and thermoplastic wires (data not shown). Focused electron-beam irradiation on PS from different sources,[11,23] indicates increase in intensity with fluence, followed by decay, marked by clear spectral red-shifting. Multiple polymers including Epoxy, PMMA, and PS have shown optical discoloration with a fluence-dependent red-shift upon gamma irradiation.[24] We note that our materials are not pure polymers and were treated according to EM sample preparation protocols. HM20 was embedded with HeLa cells after fixation with aldehydes and osmium tetroxide. The generated low energy electrons could initiate multiple chemical reactions even with a pure polymer, with other chemicals adding complexity. The question on the chemical origins of induced luminescence is outside the scope of our study, but our data in the context of literature raises two questions. i) When examined over a large fluence range and similar conditions, will multiple polymers show similar induced luminescence behavior despite their chemical dissimilarities and consequent differences in luminescence origin? ii) If multiple chemical sources of induced luminescence are possible, should attention be diverted to subtle signatures than its mere presence given how commonplace it is?

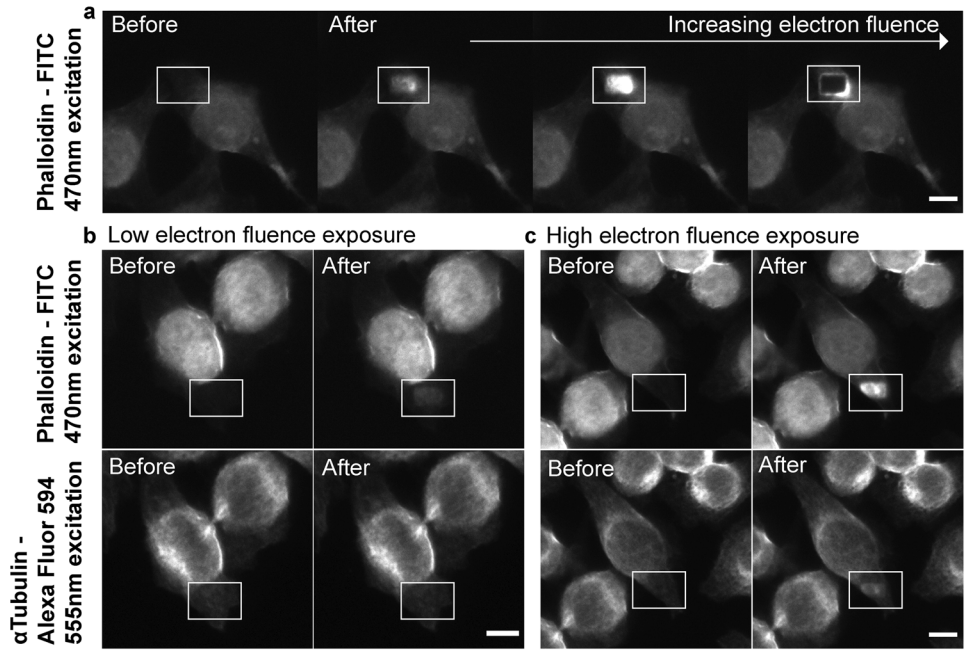

Figure 7. Electron-beam induced luminescence persists in fixed HeLa cells without embedding resin. Fixed HeLa cells labeled for Phalloidin with FITC and α-tubulin with Alexa Fluor 594 were selectively exposed to electron-beam irradiation. The solid rectangle surrounds the scanned region. a) Excitation of Phalloidin-FITC at 470 nm. Electron fluence increases from left to right, starting from zero exposure. Luminescence is clearly induced in the cellular sample upon electron exposure followed by bleaching at higher electron fluence. b,c) Excitation at 470 and 555 nm for low and high electron fluence, respectively. Left and right images show before and after electron-beam irradiation. (b) Induced luminescence grows from the blue spectral range, as observed in bare resins. For the same low electron fluence, 470 nm illumination begets higher induced luminescence while it is negligible at 555 nm. (c) Luminescence red-shifts upon higher electron fluence exposure. Scale bars: 10 µm.

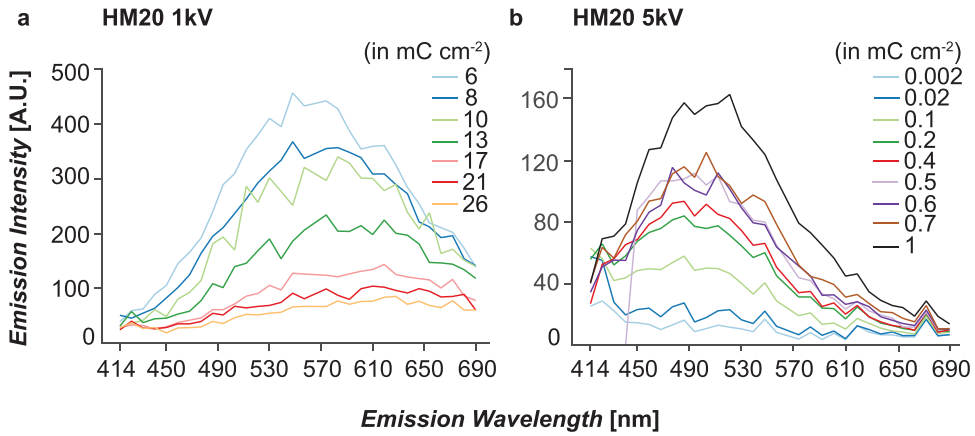

Figure 8. Comparison of electron-induced luminescence in methacrylic HM20 with literature results on PMMA.[10] Induced luminescence as a function of emission wavelength for a) 80 nm thick HM20 after irradiation with 1 keV electrons, b) with 5 keV electrons, both at 405 nm excitation. Data in (a) and PMMA[10] cover a similar range in applied electron fluence, but HM20 shows decreasing, red-shifting luminescence while PMMA shows increasing, nonshifting induced luminescence. For HM20 the interaction volume is entirely deposited in the sample, while for PMMA most scattering takes place in the underlying substrate. For HM20 at 5 keV exposure, fluences give in rough approximation similar dose deposited in the sample compared to PMMA. In this range, HM20 shows a luminescence increase that could also be approximated as spectrally nonshifting. Legends denote respective fluences in mC cm^{-2}.

2.6. Considerations for Correlative and Cathodoluminescence Microscopy

Electron-induced luminescence can impact CL measurements, where the aim is to detect luminescence from biological markers excited by a focused electron-beam. The reported exposure-dependent induced luminescence could make for a varying background that deteriorates signal detection efficiency. We note that our analysis uses photon-excited fluorescence imaging after fixed fluence electron exposure. In general, photo- and CL spectra tend

to overlap, but the efficiency for excitation with an electron-beam may be considerably lower than the photoexcitation efficiency. On the other hand, the same holds for the excitation efficiencies of CL probes and the push for smaller probes[19,25] will also considerably reduce the detectable probe signal. The broad examined fluence range is applicable to both high-resolution EM and CL probe excitation and the predictable trends across different media permit optimized probe and experimental parameter selection. However, precise determination for CL requires a thorough body of work assessing also optimized CL energies. In general, as low electron fluences do not trigger induced luminescence between 561 and 633 nm, low fluence examination, and red-excitable probes are preferred. Thin resin sections also automatically keep the background low.

Our results provide perspective in the light of recent results on electron exposure induced CL from existing fluorescent probes such as fluorescent proteins.[15] Further analysis of electron-induced luminescence origins may be required to confirm if these CL changes take place at the single probe level or result from chemical reactions between probes and/or the environment. For CLEM, the impact of electron-induced luminescence is more subtle since FM inspection typically precedes EM imaging. However, integrated systems that employ novel methods to manipulate fluorescence with an electron-beam may have to factor in and/or circumvent the effects of induced luminescence. Some examples include using the electron-beam to either selectively/permanently switch off fluorescence for localization or to generate sparsity for super-resolution approaches.[26]

Moreover, the prevalence of electron-induced luminescence in all examined resins, embedded biomaterial, and resin-devoid fixed cells could allow electron exposed biological samples to be annotated using precisely defined (size, intensity, and emission wavelength) luminescence markers (Figure 1c). This could facilitate easy optical inspection of nonfluorescent EM samples to identify and/or retrieve EM irradiated, and thus previously examinedregions, which could be particularly useful in large-scale intermittent EM imaging. Preliminary experiments reveal that even nylon microfibers from a 3D printer display visible luminescence after electron exposure (not shown). This may provide an interesting way to visualize microplastics in a fluorescence microscope. Further investigation into the involved chemical transitions and higher resolution spectral analysis as discussed above would then be of relevance.

3. Conclusion

We have spectrally (UV–Vis) characterized luminescence induced by electron-beam irradiation in two epoxy resins (Epon, Durcupan) and one methacrylate resin (HM20) over a broad electron fluence range, from 10^{-4} to 10^{3} mC cm^{-2}, both with and without embedded biological samples. We report that electron-induced luminescence is pervasive in all three bare resins, biomaterial within resin, and occurs even in fixed, whole cells in the total absence of resin. Further, we observe similar trends across all samples, with the luminescence first increasing, then red-shifting, and finally bleaching upon increasing fluence. Increased landing energies cause reduced scattering in the specimen shifting the luminescence profiles to higher fluences.

The fact that electron irradiation initiates luminescence centers in resins and biological materials is important for selecting probes and conditions for CL and CLEM. However, electron-induced luminescence also provides a means to track or mark regions of interest inspected with EM or to annotate sections for later reference. More generally, the possibility to turn many polymers into luminescent (nano) structures with tunable intensity and spectral properties is attractive and applicable to multiple fields of biology, materials science, and nanophotonics.

4. Experimental Section

80 nm thick epoxy (Epon, Durcupan) and methacrylate-based resin (HM20) sections were subjected to controlled electron fluence exposure and subsequent UV–Vis spectral characterization. Epon was examined in a bare format and thereafter again with embedded rat pancreas tissue. The rest of the samples contained embedded biomaterial. Without any labeling, the biological regions could be distinguished from the surrounding bare resin areas through differences in their electron-induced luminescence intensities. However, epoxy resins tend to copolymerize with proteins,[27] and the demarcated regions may not be representative of purely bare resin behavior. The resin type and the associated biomaterial are Epon with rat pancreas tissue and Durcupan/HM20 with HeLa cells.

Preparation of Resin Sections: For Epon (Serva electrophoresis GmbH, Germany) and Durcupan (ACM, Sigma-Aldrich), the biomaterial was first fixed with 2% paraformaldehyde and 0.2% glutaraldehyde in 0.1 M sodium cacodylate buffer, followed by postfixation with 1% osmium tetroxide and 1.5% potassium ferrocyanide in 0.1 M sodium cacodylate buffer. Subsequently, for the epoxy resins, tissue and cells were dehydrated through a graded series of ethanol and, finally, embedded in the epoxy resin which was polymerized for 24 h at 58 °C. Bare Epon blocks were created by polymerizing blocks of pure resin for 24 h at 58 °C. For HM20 embedding (Electron Microscopy Sciences, Hatfield, PA), cells were dehydrated through a graded ethanol series with lowering temperature down to −30 °C, and finally polymerized in pure HM20 by UV irradiation for 16 h at −30 °C.

Ultrathin 80 nm sections were cut from each sample using an ultramicrotome (Leica EM UC7) and placed on ITO-coated glass cover slips (Optics Balzers AG).

It is noted that for Epon bare and tissue embedded results were recorded from separate samples, whereas bare and bio-embedded regions in Durcupan and HM20 were distinguished within the same specimen.

HeLa cells were fixed with a combination of 2.5% paraformaldehyde and 1.25% glutaraldehyde, labeled with Phalloidin-FITC (Invitrogen, F432) and immunolabeled against αTubulin (Sigma, T6074) with Alexa Fluor 594 (Invitrogen, A21207), and dehydrated through a graded ethanol series.

Electron Irradiation: Focused electron-beam irradiation was carried out in a Thermo Fisher Scientific Verios SEM retrofitted with a Delmic SECOM[28] for in situ fluorescence microscopy. Exposures were conducted at a chamber pressure of $\approx 5 \times 10^{-4}$ Pa. The resin sections were markedly visible in the SEM-SECOM under UV illumination at 405 nm (Figure 1). Subsequent navigation was hence possible without unnecessary electron-beam exposure. However, polymers and chiefly epoxy derivatives are susceptible to UV photodegradation,[29] hence the illumination power and duration were kept to a minimum.

Before irradiation, the beam currents were measured using a Faraday cup (Thermo Scientific system standard test sample) via a picoammeter. The applied fluence is calculated as follows

$$\text{Fluence} = \frac{\text{Measured current} * \text{Dwell time} * \text{Scan resolution}}{\text{Irradiated area}} \quad (1)$$

where the dwell time refers to the electron-beam dwell time per exposed pixel.

Samples were exposed at 1 and 5 kV landing energies with total fluence in the range of 10^{-4} to 10^{3} mC cm^{-2}. This large range was chosen to sweep the entire spectrum inclusive of luminescence induction, rise and subsequent bleaching. Each fluence was applied on a rectangular area of 50 µm by 30 µm, in a meandering fashion with increasing fluence from the top-left to bottom right. In poorly conducting specimens like these, beam deflection due to charge accumulation is likely.[30] However, this, does not influence the central irradiated region, where the integrated fluence is unaffected. The fluence lost to the edges is marginal compared to that deposited in the ROI (area: 1500 µm^2) and is thus ignored.

UV–Vis Spectral Characterization: The UV–Vis emission of electron-beam irradiated resins was spectrally characterized at five excitation wavelengths (405, 488, 561, 594, and 633 nm) using a laser scanning confocal system (Zeiss LSM 780, Plan-Apochromat 63×/1.40 lens). Emission spectra were recorded with lambda mode creating intensity profiles between 414 and 690 nm at 9 nm intervals for each excitation with appropriate beam splitters. The illumination power per excitation was set at 6.5, 5.5, 16, 15, and 13 µW from 405 to 633 nm, respectively. The results were scaled to the power at 405 nm to make the emission intensities comparable. The detector's analog/digital gain and offset were constant, with the pinhole held completely open. The same settings were applied to every examined resin.

Supporting Information

Supporting Information is available from the Wiley Online Library or from the author.

Acknowledgements

The authors acknowledge the financial support of the Dutch Research Council (NWO) (TTW – OTP Project No. 15313), ZonMW 91111.006, NWO 175-010-2009-023, and STW "Microscopy Valley" 12718. The labs of J.P.H. and B.N.G.G. were supported by the National Roadmap for Large-Scale Research Infrastructure (Project No. 184.034.014) "Netherlands Electron Microscopy Infrastructure" (NEMI), which was financed in part by NWO.

Conflict of Interest

The authors declare no conflict of interest.

Data Availability Statement

Research data are not shared.

Keywords

cathodoluminescence, correlative light and electron microscopy, electron-beam induced luminescence, electron-beam irradiation, embedding resins, polymer luminescence, radiation damage

Received: June 21, 2021
Revised: August 16, 2021
Published online:

[1] A. J. Koster, J. Klumperman, *Nat. Rev. Mol. Cell Biol.* **2003**, *4*, 6.
[2] A. Chapiro, *Nucl. Instrum. Methods Phys. Res., Sect. B* **1988**, *32*, 111.
[3] J. H. O'Donnell, in *Radiation Effects on Polymers* (Eds: R. L. Clough, S. W. Shalaby), American Chemical Society, Washington, DC, USA **1991**, Ch. 24.
[4] K. Dawes, L. C. Glover, D. A. Vroom, *Phys. Prop. Polym. Handb.* **2007**, 867.
[5] C. Kizilyaprak, G. Longo, J. Daraspe, B. M. Humbel, *J. Struct. Biol.* **2015**, *189*, 135.
[6] R. Skoupy, J. Nebesarova, M. Slouf, V. Krzyzanek, *Ultramicroscopy* **2019**, *202*, 44.
[7] E. Kim, J. Kyhm, J. H. Kim, G. Y. Lee, D. H. Ko, I. K. Han, H. Ko, *Sci. Rep.* **2013**, *3*, 3.
[8] A. Quaranta, *Nucl. Instrum. Methods Phys. Res., Sect. B* **2005**, *240*, 117.
[9] H. Nakamura, Y. Shirakawa, S. Takahashi, H. Shimizu, *EPL* **2011**, *95*, 22001-p1.
[10] C. A. Barrios, S. Carrasco, V. Canalejas-Tejero, D. López-Romero, F. Navarro-Villoslada, M. C. Moreno-Bondi, J. L. G. Fierro, M. C. Capel-Sánchez, *Mater. Lett.* **2012**, *88*, 93.
[11] H. M. Lee, Y. N. Kim, B. H. Kim, S. O. Kim, S. O. Cho, *Adv. Mater.* **2008**, *20*, 2094.
[12] P. Wang, Z. Li, L. Zhang, L. Tong, **2013**, *38*, 1040.
[13] Y. K. Hong, D. H. Park, S. K. Park, H. Song, D.-C. Kim, J. Kim, Y. H. Han, O. K. Park, B. C. Lee, J. Joo, *Adv. Funct. Mater.* **2009**, *19*, 567.
[14] K. Nagayama, T. Onuma, R. Ueno, K. Tamehiro, H. Minoda, *J. Phys. Chem. B* **2016**, *120*, 1169.
[15] K. Akiba, K. Tamehiro, K. Matsui, H. Ikegami, H. Minoda, *Sci. Rep.* **2020**, *10*, 17342.
[16] H. Zhang, D. R. Glenn, R. Schalek, J. W. Lichtman, R. L. Walsworth, *Small* **2017**, *13*, 1700543.
[17] S. R. Hemelaar, P. De Boer, M. Chipaux, W. Zuidema, T. Hamoh, F. Perona Martinez, A. Nagl, J. P. Hoogenboom, B. N. G. Giepmans, R. Schirhagl, *Sci. Rep.* **2017**, *7*, 720.
[18] D. R. Glenn, H. Zhang, N. Kasthuri, R. Schalek, P. K. Lo, A. S. Trifonov, H. Park, J. W. Lichtman, R. L. Walsworth, *Sci. Rep.* **2012**, *2*, 865.
[19] M. B. Prigozhin, P. C. Maurer, A. M. Courtis, N. Liu, M. D. Wisser, C. Siefe, B. Tian, E. Chan, G. Song, S. Fischer, S. Aloni, D. F. Ogletree, E. S. Barnard, L.-M. Joubert, J. Rao, A. P. Alivisatos, R. M. Macfarlane, B. E. Cohen, Y. Cui, J. A. Dionne, S. Chu, *Nat. Nanotechnol.* **2019**, *14*, 420.
[20] W. Zhang, L. G. D. A. Melo, A. P. Hitchcock, N. Bassim, *Micron* **2019**, *120*, 74.
[21] S. Bakhshandeh, H. M. Taïeb, R. Schlüßler, K. Kim, T. Beck, A. Taubenberger, J. Guck, A. Cipitria, *Soft Matter* **2021**, *17*, 853.
[22] L. Reimer, *Scanning Electron Microscopy: Physics of Image Formation and Microanalysis*, Springer, Berlin **1985**.
[23] Y. Kamura, K. Imura, *Appl. Phys. Lett.* **2018**, *112*, 243104-1.
[24] R. L. Clough, K. T. Gillen, G. M. Malone, J. S. Wallace, *Radiat. Phys. Chem.* **1996**, *48*, 583.
[25] K. Keevend, R. Krummenacher, E. Kungas, L. R. H. Gerken, A. Gogos, M. Stiefel, I. K. Herrmann, *Small* **2020**, *16*, 2004615.
[26] R. I. Koning, A. Srinivasa Raja, R. I. Lane, A. J. Koster, J. P. Hoogenboom, in *Correlative Imaging: Focusing on the Future* (Eds: P. Verkade, L. M. Collinson), John Wiley & Sons, New York **2019**, pp. 119–135.
[27] J.-D. Acetarin, E. Carlemalm, E. Kellenberger, W. Villiger, *J. Electron Microsc. Tech.* **1987**, *6*, 63.
[28] A. C. Zonnevylle, R. F. C. Van Tol, N. Liv, A. C. Narvaez, A. P. J. Effting, P. Kruit, J. P. Hoogenboom, *J. Microsc.* **2013**, *252*, 58.
[29] A. Ghasemi-Kahrizsangi, J. Neshati, H. Shariatpanahi, E. Akbarinezhad, *Prog. Org. Coat.* **2015**, *85*, 199.
[30] K. T. Arat, T. Klimpel, A. C. Zonnevylle, W. S. M. M. Ketelaars, C. T. H. Heerkens, C. W. Hagen, *J. Vac. Sci. Technol., B* **2019**, *37*, 051603.